

# Galaxy formation on the largest scales: The impact of astrophysics on the BAO peak

R. E. Angulo<sup>1,2,3</sup> \*, S. D. M. White<sup>3</sup>, V. Springel<sup>4,5</sup>, B. Henriques<sup>3</sup>

<sup>1</sup> *Centro de Estudios de Física del Cosmos de Aragón, Plaza San Juan 1, Planta-2, 44001, Teruel, Spain.*

<sup>2</sup> *Kavli Institute for Particle Astrophysics and Cosmology, Stanford University, SLAC National Accelerator Laboratory, Menlo Park, CA 94025, USA*

<sup>3</sup> *Max-Planck-Institute for Astrophysics, Karl-Schwarzschild-Str. 1, 85740 Garching, Germany.*

<sup>4</sup> *Heidelberg Institute for Theoretical Studies, Schloss-Wolfsbrunnengasse 35, 69118, Heidelberg, Germany,*

<sup>5</sup> *Zentrum für Astronomie der Universität Heidelberg, ARI, Mönchhofstr. 12-14, 69120 Heidelberg, Germany.*

22 August 2018

## ABSTRACT

We investigate the effects of galaxy formation on the baryonic acoustic oscillations (BAO) peak by applying semi-analytic modelling techniques to the Millennium-XXL, a  $3 \times 10^{11}$  particle N-body simulation of similar volume to the future EUCLID survey. Our approach explicitly incorporates the effects of tidal fields and stochasticity on halo formation, as well as the presence of velocity bias, spatially correlated merger histories, and the connection of all these with the observable and physical properties of galaxies. We measure significant deviations in the shape of the BAO peak from the expectations of a linear bias model built on top of the nonlinear dark matter distribution. We find that the galaxy correlation function shows an excess close to the maximum of the BAO peak ( $r \sim 110h^{-1}\text{Mpc}$ ) and a deficit at  $r \sim 90h^{-1}\text{Mpc}$ . Depending on the redshift, selection criteria and number density of the galaxy samples, these bias distortions can be up to 5% in amplitude. They are, however, largely absorbed by marginalization over nuisance parameters in current analytical modelling of the BAO peak in configuration space, in particular into the parameter that controls the broadening due to nonlinear evolution. As a result, the galaxy formation effects detected here are unlikely to bias the high-precision measurements planned by the upcoming generation of wide-field galaxy surveys.

**Key words:** cosmology:theory - large-scale structure of Universe.

## 1 INTRODUCTION

The simple  $\Lambda\text{CDM}$  cosmological model has been supported consistently over the last 20 years by virtually every observational probe. Measurements of the cosmic microwave background (CMB), large-scale structure (LSS), type-Ia supernovae, the Ly- $\alpha$  forest, weak gravitational lensing, and the abundance of galaxy clusters, all seem to point towards the existence of dark energy and dark matter, with a cosmology based on ordinary general relativity and Gaussian primordial density fluctuations (e.g. Komatsu et al. 2011; Sánchez et al. 2012; Beutler et al. 2012; Suzuki et al. 2012; Fu et al. 2008; Rozo et al. 2010; Planck Collaboration et al. 2013; Viel et al. 2013). This overwhelming and diverse observational evidence is, nevertheless, still not fully conclusive, and the lack of any convincing independent indication of the nature of either dark matter or dark energy has fu-

eled many observational campaigns to provide more precise tests further test of  $\Lambda\text{CDM}$  predictions (e.g. DES, HETDEX, J-PAS, MS-DESI, CHIME, TAIPAN, Euclid, LSST). The discovery of any departure from the vanilla  $\Lambda\text{CDM}$  model would help us to understand better the dominant constituents of our Universe.

One of the simplest astrophysical observations – measuring the redshift and angular position of galaxies on the sky – provides one of the most powerful ways to constrain the cosmological model. Statistical measurements of the spatial distribution of galaxies can be compared with theoretical models and, in this way, can be used to derive constraints on the parameters of a given cosmological model. This exercise is most commonly done on large scales (but see Cacciato et al. 2013; Simha & Cole 2013). In particular, some of the strongest current constraints on the expansion history arise from measurements of the position of a particular feature of scale  $\sim 110h^{-1}\text{Mpc}$ : the Baryonic Acoustic Oscillation (BAO) peak (Eisenstein et al. 2005; Cole et al.

\* rangulo@stanford.edu

2005; Blake et al. 2011; Beutler et al. 2011; Anderson et al. 2012).

A fundamental assumption underpinning the extraction of cosmological information from such measurements is that, on large scales, the complex astrophysical processes responsible for galaxy formation can be decoupled from gravity and represented by a set of nuisance parameters, thus allowing the galaxy abundance in a given volume element to be related directly to the underlying primordial mass density, which, in turn, can be described using linear perturbation theory. In this way, a working description of the observables can be built and cosmological constraints can be derived.

This simplified picture may, however, be too crude to obtain precise results. The underlying dark matter (DM) density field differs nontrivially from that expected in linear theory. Nonlinear effects due to mode coupling weaken and distort the BAO peak. Nonlinear evolution also breaks the simple relation between density and velocity divergence predicted by linear theory, with implications for the measurement of clustering from redshifts which reflect both the Hubble flow and the peculiar velocities of galaxies: these so-called “redshift space distortions” (RSD) further weaken the BAO peak. Finally, the relation between the mass density field and the galaxy distribution is complex. In particular, galaxies trace the underlying field in a biased manner because they form at the bottom of local potential wells (the centres of DM haloes) not at the locations of random DM elements. This may imply that they trace the underlying velocity field in a special way too, introducing velocity biases. Moreover, halo formation is a function not only of the local DM density, but also of the tidal field and other aspects of the local environment. Finally, the relation between DM haloes and the galaxies they contain is not set at their observed redshift, but rather reflects their entire assembly history. This has particularly marked effects on satellite galaxies.

The effects of nonlinear evolution and redshift space distortion on the BAO signal in the DM and halo distributions have been studied and quantified extensively in recent years (Seo & Eisenstein 2003; Angulo et al. 2005; Seo & Eisenstein 2005; Angulo et al. 2008a; Smith et al. 2008; Sánchez et al. 2008; Seo et al. 2010). They have been shown to shift the location of the BAO peak and, if uncorrected, to bias estimates of cosmological parameters. In comparison, the impact of galaxy formation has been much less explored. This reflects the difficulty in estimating its effects theoretically. State-of-the-art  $N$ -body simulations are just beginning to achieve the volume and mass resolution required to follow the assembly of the haloes expected to host typical galaxies over the volumes to be targeted by upcoming surveys (Kim et al. 2011; Angulo et al. 2012b; Watson et al. 2013). *Ab initio* hydrodynamical simulations of galaxy formation over the required volumes are still far beyond current computational capabilities.

Our limited understanding of the effects of galaxy formation on the BAO signal contrasts with the importance of the topic. The extraction of robust and precise information about the dark energy from future galaxy surveys will rely critically on a quantitative understanding of this issue.

In this paper, we perform the most realistic modelling of the galaxy population on large scales to date, explicitly showing that BAO measurements in configuration and

redshift space can indeed be affected by galaxy formation physics. We do this by combining a large DM only  $N$ -body simulation with a post-processing scheme for simulating galaxy formation. The first of these ingredients follows self-consistently the nonlinear growth of structure, the formation of self-bound objects, their connection to the velocity and tidal fields, and their evolution over cosmic time. The second couples a collection of physically motivated equations capturing the many processes relevant for galaxy formation to the accretion, merger history and dynamics of the DM halos and subhalos. We note that this procedure explicitly takes into account the assembly history of each DM halo and its correlation with the surrounding large-scale overdensity field.

These tools allow us to show explicitly that galaxy clustering on very large scales, and the BAO peak in particular, is not a linearly scaled version of DM clustering, as is often assumed. Deviations from this model are small, but will nevertheless have to be understood quantitatively in order to fully exploit future clustering measurements, and are thus a requirement if they are to fulfil their promise as robust and precise probes of the dark energy equation of state and the nature of the gravity law.

The layout of this paper is the following. First, in Section 2.1 we present the  $N$ -body simulation used for this work, and in Section 2.2 we give a brief summary of the main features of our semi-analytic model for galaxy formation. In Section 2.3 we describe the implementation of this model on our  $N$ -body simulation and how we overcame problems due to its relatively poor mass resolution. We present our main results in Section 3 and 4, focusing first on the connection between individual haloes and their galaxies, and then on an exploration of clustering statistics. Finally, we conclude in Section 5.

## 2 METHODS

### 2.1 The MXXL $N$ -body simulation

The  $N$ -body simulation used for this paper, Millennium-XXL (MXXL), is the latest member of the Millennium Simulation series (Springel et al. 2005; Boylan-Kolchin et al. 2009, MS, MS-II). Extensive details of the simulation were given in Angulo et al. (2012b,a). Here we just provide a short description of the main features relevant for this work.

The MXXL uses  $6720^3$  particles, each of mass  $m_p = 6.1 \times 10^9 h^{-1} M_\odot$ , to simulate the growth of cosmic structure over a volume of  $V = 27 (h^{-1} \text{Gpc})^3$ . This combination of mass resolution and volume is adequate to obtain good statistical precision on the scales relevant for BAO and RSD measurements, while resolving the halos and subhalos expected to host the galaxies targeted by next-generation, large-volume surveys. The cosmological parameters and output times were set to match those of the two previous Millennium simulations, specifically,  $h = 0.73$ ,  $\Omega_m = 0.25$ ,  $\Omega_\Lambda = 0.75$ ,  $n = 1$  and  $\sigma_8 = 0.9$ . Halo/subhalo catalogues are stored for 63 snapshots, roughly spaced by 300 Myr at  $z \sim 0$ . The cosmological parameters differ from those preferred by more recent cosmological analyses (see Angulo & White 2010, for a way to adjust for this), however, this has little importance for predicting the spatial distribution of the

galaxy population as shown by Guo et al. (2013a). The initial conditions were generated at  $z = 63$ , which ensures that artificial transients are negligible for low-redshift clustering statistics (Angulo et al. 2008a).

At each snapshot, haloes with more than 20 particles were identified by a FoF algorithm (Davis et al. 1985), and self-bound subhaloes with more than 15 particles were found using SubFind (Springel et al. 2005). Both of these operations were performed on-the-fly during the  $N$ -body calculation, which reduced significantly the overall I/O workload and disk usage.

Subhalo merger trees were built subsequently by identifying, for each subhalo in each snapshot, the most likely descendant in the following snapshot. This was done by tracking the 15 most bound particles of the subhalo, giving them a weight proportional to  $j^{-2/3}$ , where  $j$  is the particle position in a list ordered by binding energy. This approach gives more importance to the particles expected to best represent the orbit of hypothetical galaxies. We note that our tree-building scheme is slightly simpler than that employed for the MS (for instance, we do not perform backwards checks on the descendants, nor look for descendants more than one snapshot ahead). We have, however, explicitly checked that this has no impact on the quantities explored in this paper.

Using these procedures, we constructed 600 million distinct trees with a root halo at  $z = 0$ , containing a total of over 25 billion nodes. These structures are the backbone of our modelling of the galaxy population in the MXXL.

## 2.2 The semi-analytic model of galaxy formation

In this paper, the properties of galaxies within our simulated volume will be generated using the semi-analytic galaxy formation code *L-Galaxies* (Springel et al. 2005). This code couples the (sub)halo merger trees described in the previous subsection (from which the mass growth, dynamics and spatial distribution are taken), with a system of differential equations that encode the key physical mechanisms for galaxy formation. In particular, processes such as gas cooling, star formation, feedback from SN and AGN, galaxy mergers, black hole formation and growth, and generation of metals are all implemented in a self-consistent manner. The philosophy and methods of semi-analytic models can be found in the review of Baugh (2006), whereas specific aspects of recent versions of *L-Galaxies* are described in full detail by Guo et al. (2011), Henriques et al. (2012) and references therein. Here, we simply note that this model successfully reproduces many (though certainly not all) observable properties of high and low- $z$  galaxies.

Most important for this paper is the fact that our framework is physically consistent. All galaxy formation takes place at the centres of DM subhalos. Further, the galaxy population of a given DM halo does not depend on its mass alone, as assumed in most Halo Occupation Distribution (HOD) models, but also on the details of the halo’s assembly history. Thus, a recently-formed halo will typically contain a central galaxy with younger stars than a halo of similar mass which formed earlier, and galaxies with strong AGN activity are typically found in more massive halos than galaxies of similar stellar mass which are not active. (This is because feedback from the black hole effectively decouples galaxy growth from halo growth in the active case.) Such processes

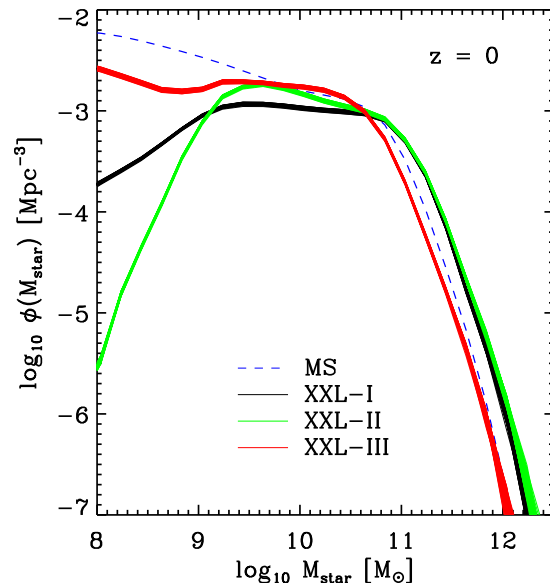


**Figure 1.** The present-day stellar mass function predicted by a semi-analytic code for galaxy formation applied to dark matter only  $N$ -body simulations. The dashed line shows the result for the MS, while solid lines show three predictions for the MXXL: The black line is based on the original *L-Galaxies* code, without any corrections for the finite resolution of the MXXL. For the green line, each leaf in our merger trees was initialised with MS galaxies from a halo of similar mass and redshift. For the final MXXL model (shown in red) we also included (statistically) mergers which are unresolved in the MXXL. Note that these modifications progressively improve the agreement between the MS and the MXXL. In the MXXL case, we display 216 different curves, each representing a cubic subregion with the same volume as the MS.

connect the large-scale environment with galaxy properties and may produce observable effects in wide-field galaxy surveys.

The complex relation between DM and galaxies implies that a galaxy sample selected according to specific observable properties will not, in general, be simply a scaled version of the underlying DM field, nor even correspond to the halo distribution weighted by an average mass-dependent occupation number. Instead, such samples contain non-trivial correlations between scales, and between the mass distributions at different times. These may be manifest, for instance, as an “assembly” bias (Gao et al. 2005; Wechsler et al. 2006; Gao & White 2007; Croton et al. 2007; Angulo et al. 2008b) or as a distortion in the appearance of the large-scale structure (e.g. Bower et al. 1993). These possibilities demonstrate the importance of a realistic model for galaxy formation, capable of quantifying how such effects bias measurements of cosmological parameters from galaxy clustering observations.

## 2.3 Implementation

The MXXL is the highest resolution simulation of the Universe on very large scales, yet its mass resolution is not high enough for the semi-analytic code to produce results con-

vergent with those of the higher resolution MS/MS-II. This is true even for the most massive galaxies expected in our simulation volume. The disagreement can be seen by comparing the black solid and blue dashed lines in Fig. 1, which shows  $\phi$ , the number of galaxies per logarithmic stellar mass bin and per unit volume. The relatively small difference in mass resolution (a factor of  $\sim 7$ ) allows the MS to model galaxies reliably to a hundred times lower mass than in the MXXL – this is a consequence of the steep relation between halo mass,  $M_{200}$ , and stellar mass,  $M_{\text{star}}$ , over the relevant range of halo masses. Compared to the MS, galaxies in the MXXL are less massive below  $M^*$  (the knee of the stellar mass function), and more massive above  $M^*$ .

There are two main reasons for these differences in stellar mass function shape. Both stem from the fact that the minimum halo mass resolved by our simulation is  $1.22 \times 10^{10} h^{-1} M_{\odot}$ , which means that halos of this mass almost never have a resolved progenitor in the MXXL merger trees. Although not shown here, we explicitly checked the fraction of haloes with no progenitors (“leaves”) in the MXXL, as a function of halo mass and time. At high redshift, virtually every halo below  $10^{11} h^{-1} M_{\odot}$  is a leaf. At lower redshifts, the fraction decreases to about 20%, because such halos are then growing much more slowly. When the original semi-analytic code encounters a leaf, it assumes that it is filled with pristine gas, shock-heated to the virial temperature. However, hydrogen can cool efficiently at the temperatures corresponding to minimum mass MXXL halos, so that such objects should, in fact, already contain galaxies at the first time they are identified. The absence of these objects explains why low-mass galaxies (below  $M_{\text{star}} \sim 10^{11} h^{-1} M_{\odot}$ ) are less abundant in the MXXL than in the MS. In addition, in halos of any given (low) mass, MXXL galaxies are typically less massive than MS galaxies because they have been forming stars for less time.

In order to solve this problem, we have modified the semi-analytic code so that instead of initialising a “leaf” with hot gas alone, we include a galaxy population taken from a MS halo of similar FoF mass and redshift. In particular, we randomly chose a MS halo at the same snapshot and with a tolerance in mass of  $\Delta \log_{10} M = 0.1$ . (We progressively increase this tolerance up to 2 when there are no matches, as is sometimes the case at high redshift for massive leaves.) The stellar mass function after this modification is shown by green lines in Fig. 1. It is clear that the increased abundance of galaxies below  $M^*$  brings the galaxy population in the MXXL much closer to that of the MS. However, a discrepancy persists at high mass.

This disagreement is again a consequence of mass resolution, but this time it is caused by the lack of minor mergers onto more massive haloes in the MXXL (those events involving accreted haloes in the mass range  $[1.7 - 12.2] \times 10^{10} h^{-1} M_{\odot}$ , i.e. between  $[0.2 - 20]$  particles). Although these missing mergers typically contain low mass galaxies ( $M_{\text{star}} < 10^9 h^{-1} M_{\odot}$  at  $z = 0$  in the MS), they have a noticeable cumulative impact on the most massive galaxies that our model predicts. In particular, and contrary to a naive expectation, the net effect of these mergers is not to increase but to decrease the stellar mass of central galaxies. Although the accreted subhaloes add stars and gas to the central galaxies, their main effect is to increase the efficiency of AGN feedback by increasing the mass of the central su-

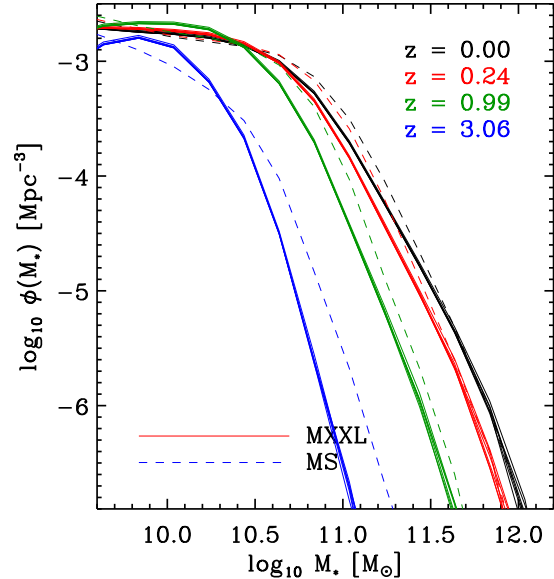


**Figure 2.** Comparison of the stellar mass functions at different redshifts for semi-analytic simulations of galaxy formation in the MXXL (solid lines) and MS (dashed lines).

permissive black holes. The more massive a BH, the more energy it will inject into surrounding gas, thereby preventing it from cooling and turning into stars.

In order to mimic the effect of unresolved mergers, we have artificially extended our merger trees by adding branches with mass below the resolution limit of the MXXL. The number of extra branches is drawn from a Poisson distribution with mean equal to the average number of low-mass mergers per halo found in the MS. Typically, the number of added mergers per halo ranges from  $\sim 0.02$  to  $\sim 50$ , for haloes of mass  $10^{11} h^{-1} M_{\odot}$  to  $10^{15} h^{-1} M_{\odot}$  at  $z = 0$ , respectively. We repeat this for every simulation snapshot and in 8 halo mass bins equally spaced in  $\log M$ . The spatial position of these new nodes follows a Lorentzian distribution with mean equal to the virial radius of the main host halo (this is consistent with direct measurements in the MS). Note that this modification is coupled with that discussed before, i.e. these new haloes contain statistically the correct galaxies.

The resulting stellar mass function is displayed by red lines in Fig. 1. This latest modification reduces the abundance of very massive galaxies, as discussed above, yielding better convergence between MXXL and MS predictions for galaxies with stellar masses above  $2 \times 10^9 h^{-1} M_{\odot}$ . In addition, we find a net increase in the number of galaxies below  $M^*$  due to the addition of a population of low-mass satellites in the range  $10^7 < M_{\text{star}}/(h^{-1} M_{\odot}) < 10^9$ , which would otherwise be absent in the MXXL. Discrepancies of up to a few tens of percent still remain at stellar masses  $\sim 10^{11} h^{-1} M_{\odot}$  but for the purposes of this paper we regard these as acceptable.

This shows that, despite the limited resolution of the MXXL, galaxy formation can be modelled in a way that leads to realistic abundances at  $z = 0$  for galaxies with  $M_{\text{star}} > 2 \times 10^9 h^{-1} M_{\odot}$ . In Figure 2, we compare stellar mass functions in the two simulations at higher redshift, focusing

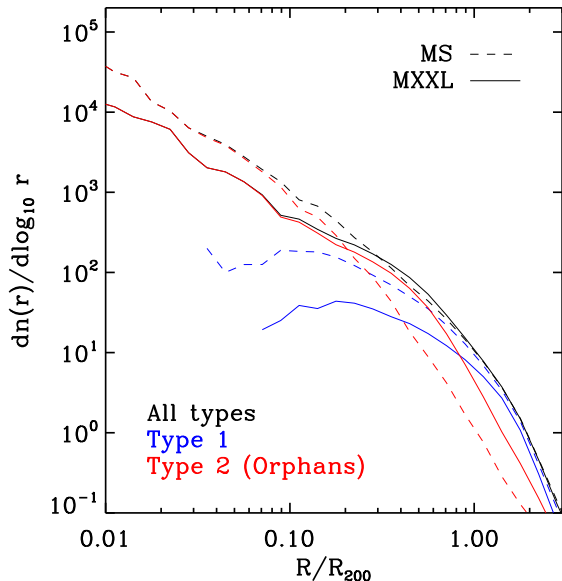


**Figure 3.** Average number density profile for the 40 satellite galaxies with the largest stellar mass inside clusters in the mass range  $2 \times 10^{14} < M/(M_{\odot}) < 5 \times 10^{14}$ . Solid lines show results for the MS, whereas dashed lines show results for the MXXL. Red and blue lines indicate the contributions of ‘type 1’ and ‘type 2’ galaxies, those which still have an associated subhalo and those which do not, respectively.

on the range of stellar masses well probed by the MXXL. We can see that there is an increasing mismatch at the high-mass end at higher redshift. Nevertheless, at  $z < 1$  the agreement is of similar quality to that at  $z = 0$ , and at all redshifts it is reasonable, if one keeps in mind that these numerical convergence errors are comparable to the observational uncertainties in stellar mass function estimates and to the systematic differences between high-redshift observational estimates and the predictions of the original Guo et al. (2011) model.

The problems discussed above highlight the importance of adequate resolution in simulations of galaxy formation. Resolution effects can be significant not only for galaxies in haloes close to the resolution limit, but also for higher mass galaxies which are substantially modified through accretion of smaller systems.

So far, we have addressed artefacts introduced by the differing mass resolution of the MXXL and the MS. The remaining difference is the inability of the MXXL to track the position of “orphan galaxies”, those whose DM subhalo has fallen below the mass resolution of the simulation due to tidal stripping. In the MS and MS-II the position of these galaxies is continuously updated using information about the position and velocity of the most bound DM particle of the galaxy’s last resolved host halo. This approach was not feasible for the MXXL, since the full particle data were stored at only a handful of redshifts in order to avoid an unmanageable data volume (following MS procedures would have produced  $\sim 1$  PetaByte). In the MXXL, once a galaxy becomes an orphan we assume that its position remains fixed relative to the central galaxy of its DM halo, except that the

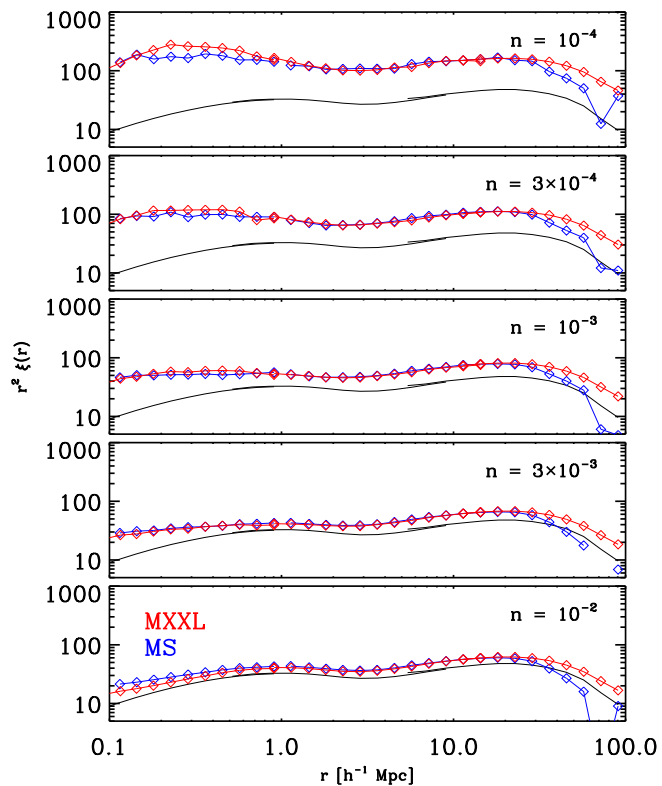


**Figure 4.** Autocorrelation functions at  $z = 0$  for galaxies in the MXXL and MS selected by stellar mass. The five panels show results for galaxy samples matching five number densities (given in the legend in units of  $h^3 \text{Mpc}^{-3}$ ). From bottom to top, they correspond to threshold stellar masses of  $1.4 \times 10^{10}$ ,  $2.7 \times 10^{10}$ ,  $5.9 \times 10^{10}$ ,  $7.3 \times 10^{10}$  and  $1.1 \times 10^{11}$  in units of  $h^{-1} M_{\odot}$ . Solid black lines denote the correlation function of DM in the MXXL.

separation linearly shrinks to mimic the effect of dynamical friction<sup>1</sup>. This has a negligible impact on the stellar mass function, but dominates the radial distribution of satellites inside halos, thus affecting small-scale galaxy clustering.

To illustrate this, in Fig. 3 we compare the average radial distribution of galaxies inside clusters of mass  $2 \times 10^{14} < M/(h^{-1} M_{\odot}) < 5 \times 10^{15}$  in the MXXL and MS. The total profiles (solid and dashed black lines) agree very well down to a scale of about  $0.4 h^{-1} \text{Mpc}$ . At smaller scales, MXXL galaxies display a core which may reflect a misestimation of the effective orbit and dynamical friction timescale for accreted subhalos. For this cluster mass, satellites with a resolved DM host are the dominant type only at relatively large distances from the cluster center,  $r > 1 h^{-1} \text{Mpc}$ . This is three times larger than the corresponding scale for the MS.

To complete this section, we compare 2-point correlation functions (2pCF) for galaxies in the MXXL and the MS – the clustering statistic most relevant for our paper. This is a demanding test, since it probes many different aspects of the simulated galaxy population, such as the way

<sup>1</sup> We note that this corresponds to the dynamical friction formula in Guo et al. (2011), not that in Guo et al. (2013b)



in which galaxies of a given property populate DM haloes, their correlation with neighbouring haloes, and their radial distribution within their own haloes.

Here and in the rest of the paper we compute the 2pCF,  $\xi(\mathbf{r})$ , in Fourier space;

$$\xi(\mathbf{r}) = \mathcal{F}^{-1} \{ \|\mathcal{F}[\delta(\mathbf{x})]\| \} \quad (1)$$

where  $\mathcal{F}$  and  $\mathcal{F}^{-1}$  respectively denote direct and inverse Fourier transforms, the vertical bars denote the modulus of a complex field, and  $\delta(\mathbf{x})$  is the input overdensity field. Operationally, we use FFTs with a mesh of  $2048^3$  cells, and a Nearest-Grid-Point assignment scheme. In addition we repeat this procedure after folding the density field 6 times in each dimension, thereby enhancing the range of scales probed. This method has the computational advantages that it is fast, and that only a subset of the objects need to be in memory at any given time. The latter is important for analyses of the MXXL due to the large number of bodies involved.

Fig. 4 shows the spherically averaged real-space 2pCF times  $r^2$  for galaxy samples selected according to their stellar mass, for five different number densities, as indicated by the figure legend. Measurements in the MXXL and in the MS agree remarkably well over the range  $0.4 < r/(h^{-1}\text{Mpc}) < 20$ , the regime where both simulations have adequate volume and resolution. On scales larger than  $20h^{-1}\text{Mpc}$ , the MS 2pCFs are systematically lower in all panels than those found for the MXXL. This is a result of the relatively small box of the MS, which does not allow correct sampling of the large-scale modes present in the MXXL. On scales smaller than  $0.4h^{-1}\text{Mpc}$ , differences arise due to the poorer spatial resolution of the MXXL and its reduced ability to track orphan galaxies, as shown in Fig. 3. In upper panels, the results for the MS are also somewhat noisy. The excellent agreement on intermediate scales validates the modifications we have implemented in our semi-analytic code, and thus the analysis we will present below.

To summarize this section, we conclude that semi-analytic galaxy formation modelling can be carried out to sufficient accuracy on the MXXL to allow construction of a realistic galaxy population. In the next two sections we will investigate further the predicted relation between the stellar mass of a galaxy and its DM host, as well as, the appearance of the BAO signal imprinted on the galaxy distribution.

### 3 THE GALAXY CATALOGUE

Within the MXXL volume at  $z = 0$ , our galaxy formation simulation predicts almost one billion galaxies with stellar mass above  $2 \times 10^9 h^{-1}M_{\odot}$ . For each of them we have followed both the evolution of its physical properties and its position and peculiar velocity, thus predicting galaxy population properties over almost five orders of magnitude in length, from one hundred kiloparsec up to 4 Gigaparsec. The full galaxy formation simulation was carried using 5000 CPU hours and produced about 5Tb of data products.

The large dynamical range covered by our galaxy catalogue can be seen in Fig. 5, which displays a projection of the distribution of galaxies at  $z = 0$  on different scales, zooming into the most massive cluster in the whole MXXL

simulation. The size and intensity with which we represent each galaxy are set by its disk diameter and its stellar mass, respectively, while the colour reflects the galaxy's star formation rate. The 50% highest star forming galaxies are depicted in blue, whereas the 50% lowest star forming are shown in red. It is evident that the galaxy distribution has similar structure to the DM distribution (see Angulo et al. 2012a, for a dark matter version of this figure), showing large clusters, filaments, sheets and voids. It is also, however, readily apparent that there are marked differences in the way in which star formation and stellar mass trace those structures and, in general, the underlying mass density field. This illustrates that different galaxy properties relate to different aspects of the cosmic web, and that galaxies do not uniformly sample the underlying DM field. We now explore quantitatively how this affects measurements of the large-scale structure of the Universe, in particular the BAO signal in the 2pCF.

Our main results will be presented in Section 4, but we begin in Section 3.1 by briefly exploring the relationship between the properties of galaxies and those of their host DM halos. This will help us to understand our later results. Then in Section 3.2 we will define the galaxy and halo samples analysed throughout the remainder of the paper.

#### 3.1 The $M_{\text{halo}} - M_{\text{star}} - M_{\text{bh}}$ relation

We start by showing in Fig. 6 the abundance of MXXL galaxies in the plane defined by halo virial mass  $M_{200}$  and stellar mass at  $z = 0$ . In the top panel we focus on central galaxies, and in the bottom panel we focus on satellites. In both cases,  $M_{\text{vir}}$  corresponds to the current mass of the host DM halo.

For central galaxies there is a monotonically increasing and tight relation between these two quantities. Above  $M_{\text{halo}} \sim 5 \times 10^{11}$ , the stellar mass of a galaxy scales roughly as the halo mass raised to the 1/3 power with a scatter of 0.2 dex. Below  $M_{\text{halo}} \sim 5 \times 10^{11}$ , the relationship is steeper:  $M_{\text{star}} \propto M_{\text{vir}}$ , with an increasing scatter. We note that the scatter in  $M_{\text{halo}}$  at a given  $M_{\text{star}}$  is significantly larger; 0.4 dex, and also displays a more complex structure.

This strong correlation between stellar mass and halo mass reflects the fact that the mass locked in stars is controlled primarily by the amount of baryonic material available in the host halo, as modulated by cooling, star formation and feedback. (As we will see in Fig. 7, the situation is more complex for the SFR.) Processes such as feedback are important in that they systematically change the overall star formation efficiency as a function of halo mass and redshift, but they only introduce scatter at fixed mass and redshift, an effect which is particularly marked in the mass range  $10^{11} < M/h^{-1}M_{\odot} < 10^{12}$ . This strong correlation is the principal justification for subhalo abundance matching techniques (e.g. Vale & Ostriker 2004).

Satellite galaxy masses are much more weakly correlated with host halo mass, as expected from hierarchical growth. However, although we do not show it here, they display the same  $M_{*} - M_{\text{halo}}$  as other central galaxies just before they are first accreted onto a more massive system, and their stellar mass evolves rather little after this time due to the relatively rapid quenching of star formation in satellites in our semi-analytic model.

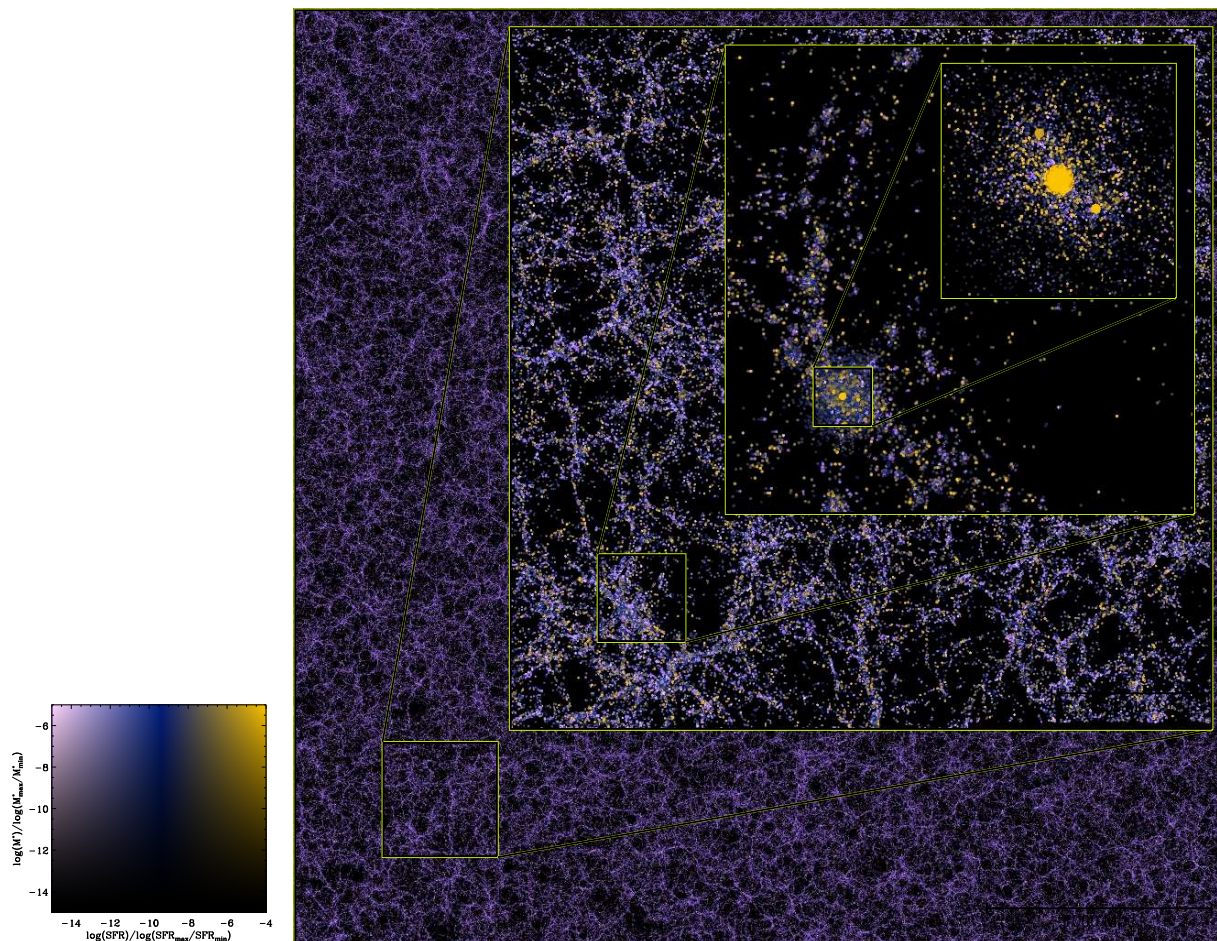


**Figure 5.** The predicted galaxy distribution in a slice of thickness 13.7 Mpc in the MXXL at  $z = 0$ . Each inset zooms by a factor of 8 from the previous one, focusing on the most massive cluster present in the simulation. The side-length varies from 4.1 Gpc down to 8.1 Mpc. Each galaxy is represented by a sphere with intensity and size related to total mass in stars and to size of the stellar disk, respectively. The intensity in the image is proportional to the logarithm of the stellar mass projected along the line-of-sight, and the colour encodes the star-formation rate weighted by the stellar mass along the line-of-sight. This simulation has a dynamic range of  $3 \times 10^5$  in each spatial dimension, simultaneously resolving the internal structure of collapsed objects and the large-scale quasi-linear fluctuations expected in a  $\Lambda$ CDM universe.

Closer inspection of this figure shows that there is increased scatter in the central galaxy relation at  $M_{\text{halo}} \sim 10^{12} h^{-1} M_{\odot}$ . This reflects the transition between two modes of galaxy growth that dominate for small and large halo masses, respectively, and that overlap at this value of  $M_{\text{halo}}$  (see Guo & White 2008).

The source of this excess scatter is further clarified in Fig. 7, which shows mean black hole mass and mean star formation rate for central galaxies as a function of their  $M_{\text{star}}$  and  $M_{\text{halo}}$ . For halo masses between  $5 \times 10^{11} h^{-1} M_{\odot}$  and  $5 \times 10^{12} h^{-1} M_{\odot}$ , deviations from the mean stellar mass, at a fixed  $M_{\text{halo}}$ , correlate with deviations in the mass of the central black hole and with the star formation rate. This is because small black holes produce less feedback, and star formation is set by cooling times and accretion onto these halos. The second population of galaxies with large black holes reaches similar star formation rates only for the most massive galaxies.

From these plots, it is clear that the relationship between galaxies and the underlying DM matter field is not simple. Galaxy properties relate to their DM haloes in a

way that depends not only on current halo state, but also on halo assembly history – through, for instance, the black hole growth history. This is particularly clear for satellite galaxies, where the galaxy-halo connection is frozen at the moment of accretion, and galaxy properties relate only weakly to the current mass either of the galaxy’s own subhalo or of its parent halo. However, this is also the case for a variety of properties of central galaxies. For example, at fixed stellar mass, red central galaxies tend to have more massive haloes than blue ones, both in the semi-analytic model and in the real world (e.g. Wang & White 2012).

### 3.2 Definition of our galaxy samples

The complexity of the galaxy-halo relationship results in variations in the large-scale clustering measured in wide-field galaxy surveys, because these follow different observational strategies and select their samples using different criteria. To explore this in our subsequent analysis, we create two samples of galaxies, one selected according to stellar mass and

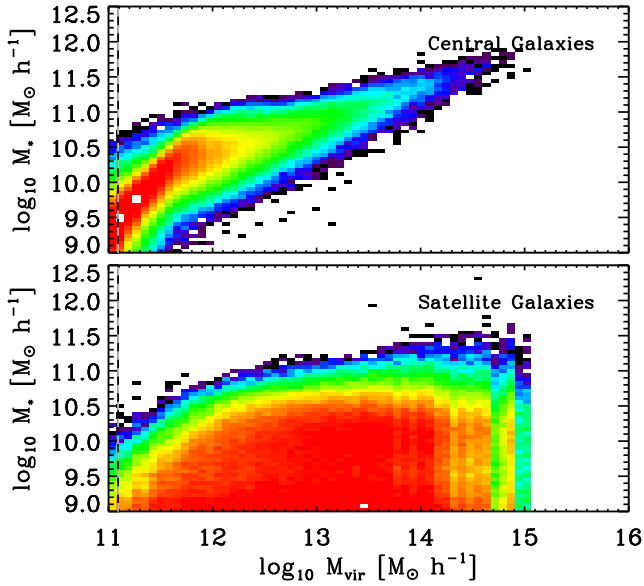


**Figure 6.** The relation between stellar mass and host halo mass for galaxies in our MXXL simulation at  $z = 0$ . For both central and satellite galaxies we use the current virial mass  $M_{200}$  of their halo. The colour in each pixel is set by the logarithm of the number of galaxies in that region of the  $M_{\text{halo}} - M_{\text{star}}$  plane, red being the highest density and black the lowest. The vertical dashed line indicates a 20 particle limit, roughly corresponding to the minimum DM halo mass resolved in our simulation.

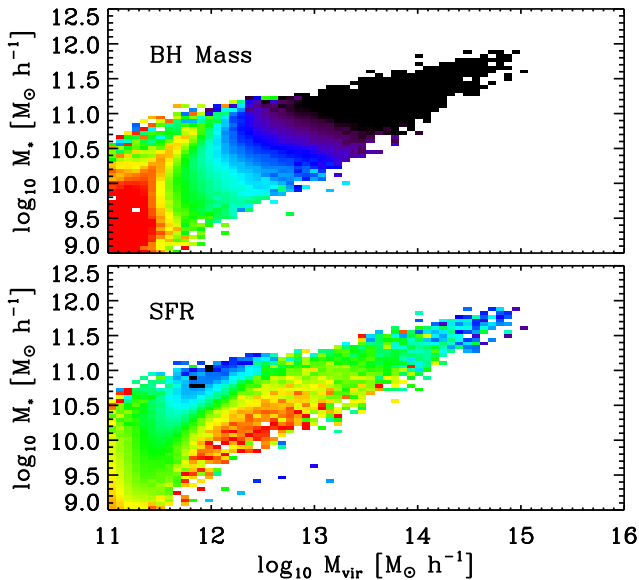


**Figure 7.** The logarithm of the average black hole mass (top) and star formation rate (bottom) for central galaxies, as a function of halo mass and stellar mass. The red color indicates a BH mass of  $2 \times 10^5 h^{-1} M_{\odot}$ , or a SFR of  $0.02 M_{\odot} \text{ yr}^{-1}$ , whereas black denotes a BH mass of  $10^9 h^{-1} M_{\odot}$  or a SFR of  $10 M_{\odot} \text{ yr}^{-1}$ , for the top and bottom panels, respectively.

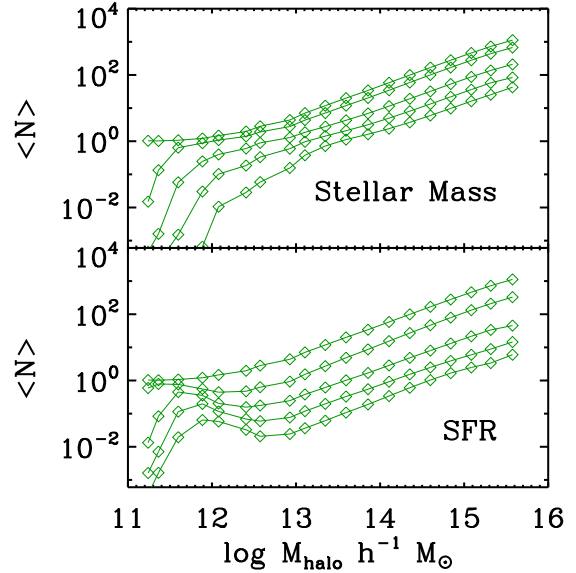


**Figure 8.** The “halo occupation distribution” (HOD), the average number of galaxies per DM halo as a function of halo mass, for galaxies in the MXXL simulation at  $z = 0$ . We show this quantity for galaxies selected according to stellar mass (top panel) and according to star formation rate (bottom panel). Different curves indicate samples at five different number densities. From top to bottom, these are  $10^{-2}$ ,  $3 \times 10^{-3}$ ,  $10^{-3}$ ,  $3 \times 10^{-4}$ ,  $10^{-4} h^3 \text{ Mpc}^3$ . Note the different shape of these curves in the two cases, especially for samples with low number density.

the other according to star formation rate, and for comparison we also select a sample of DM halos according to mass.

1) The first galaxy sample is defined using total stellar mass (i.e. the sum of the stellar mass of disk and bulge). As shown above, this property correlates quite tightly with halo mass, at least for central galaxies. Observationally, a catalogue constructed in this way mimics the selection criteria used, for example, for the CMASS sample of the BOSS survey (Eisenstein et al. 2011).

2) The second galaxy sample is defined according to instantaneous star formation rate (SFR). Since a high star formation rate implies a large number of young and massive stars, this catalogue mimics selecting galaxies by emission flux, as was done for the WiggleZ survey (Drinkwater et al. 2010), as is planned for the HETDEX experiment (Hill et al. 2008) and as is the current strategy for the EUCLID mission (Laureijs 2009). Unlike stellar mass, SFR is not expected to track halo mass closely, even for central galaxies, since starbursts can be triggered by minor mergers and by disk instabilities, and star formation can be quenched by a variety of mechanisms.

3) The third sample consists of halos selected according to their virial mass,  $M_{200}$ . This sample will help us to distinguish effects arising from the physics of galaxy formation from those that are due solely to nonlinear DM dynamics and halo identification.

For each of these three definitions, we construct samples of objects at five different number densities. In units of



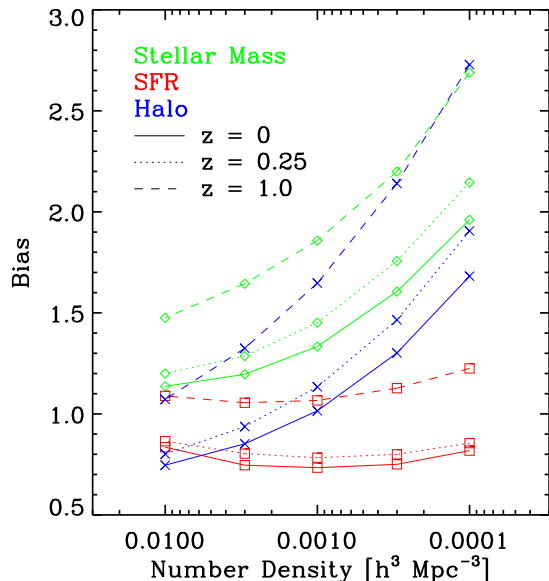


**Figure 9.** Bias as a function of number density at three redshifts for three different samples of objects; dark matter haloes selected according to their virial mass,  $M_{200}$ , galaxies selected according to their stellar mass, and galaxies selected according to their SFR. The bias is defined here as the square root of the ratio of the sample autocorrelation function to the dark matter autocorrelation function, averaged over the separation range  $60h^{-1}\text{Mpc} < r < 70h^{-1}\text{Mpc}$ .

$h^3\text{Mpc}^{-3}$ , these are  $[10^{-4}, 3 \times 10^{-4}, 10^{-3}, 3 \times 10^{-3}, 10^{-2}]$ , which for the XXL volume corresponds to 2.7, 8.1, 27, 81 and 270 million objects, respectively. For comparison, note that the CMASS sample of the BOSS survey was designed to have a roughly constant space density of galaxies,  $n = 3 \times 10^{-4} h^3\text{Mpc}^{-3}$ , that the space density of galaxies in WiggleZ is about  $n = 2 \times 10^{-4} h^3\text{Mpc}^{-3}$ , and that for the planned EUCLID survey, estimated densities range from 0.15 to  $4.8 \times 10^{-3} h^3\text{Mpc}^{-3}$ , depending on the redshift and galaxy population targeted (di Porto et al. 2012). For J-PAS, the number density of galaxies with highly-accurate photometric redshift is expected to range between  $10^{-3}$  and  $10^{-2} h^3\text{Mpc}^{-3}$ .

The average number of galaxies per DM halo in our ten galaxy samples is shown in Fig. 8. The top panel displays results for stellar-mass selected samples, whereas the bottom panel displays results for SFR-selected samples. Note the non-monotonic behaviour of the HOD for high-density samples of SFR-selected galaxies. This is consistent with the previous discussion: the abundance of star-forming galaxies is not tightly correlated with host halo mass.

In Fig. 9 we show clustering bias for all fifteen of our samples. Many different effects are visible in this plot. The bias of stellar mass-selected galaxies increases strongly with decreasing number density. The slope is almost as steep as for mass-selected DM haloes, but the overall bias is larger. This behaviour reflects the strong correlation between stellar mass and host halo mass, together with the presence of satellites in the galaxy sample. These are almost always found in haloes more massive than those surrounding cen-

tral galaxies of similar stellar mass. The presence of satellites thus increases the bias. A decrease in the satellite fraction with decreasing number density and increasing redshift explains the increasingly similar bias values for stellar mass-selected galaxies and for DM haloes at higher redshift and lower space density.

Star-forming galaxies show a very different behaviour. Although they also populate more strongly biased haloes at higher redshift, there is almost no dependence of bias on the number density of the sample. This is a consequence of the effect already seen in Fig. 7. There is very little tendency for SFR to increase with halo mass. In addition, as can be seen from Fig. 8 the satellite fraction is significantly smaller in SFR-selected samples than in stellar mass-selected samples.

## 4 LARGE-SCALE GALAXY CLUSTERING

We now study how the complex relation between the galaxy and DM distributions may affect BAO measurements from future galaxy surveys

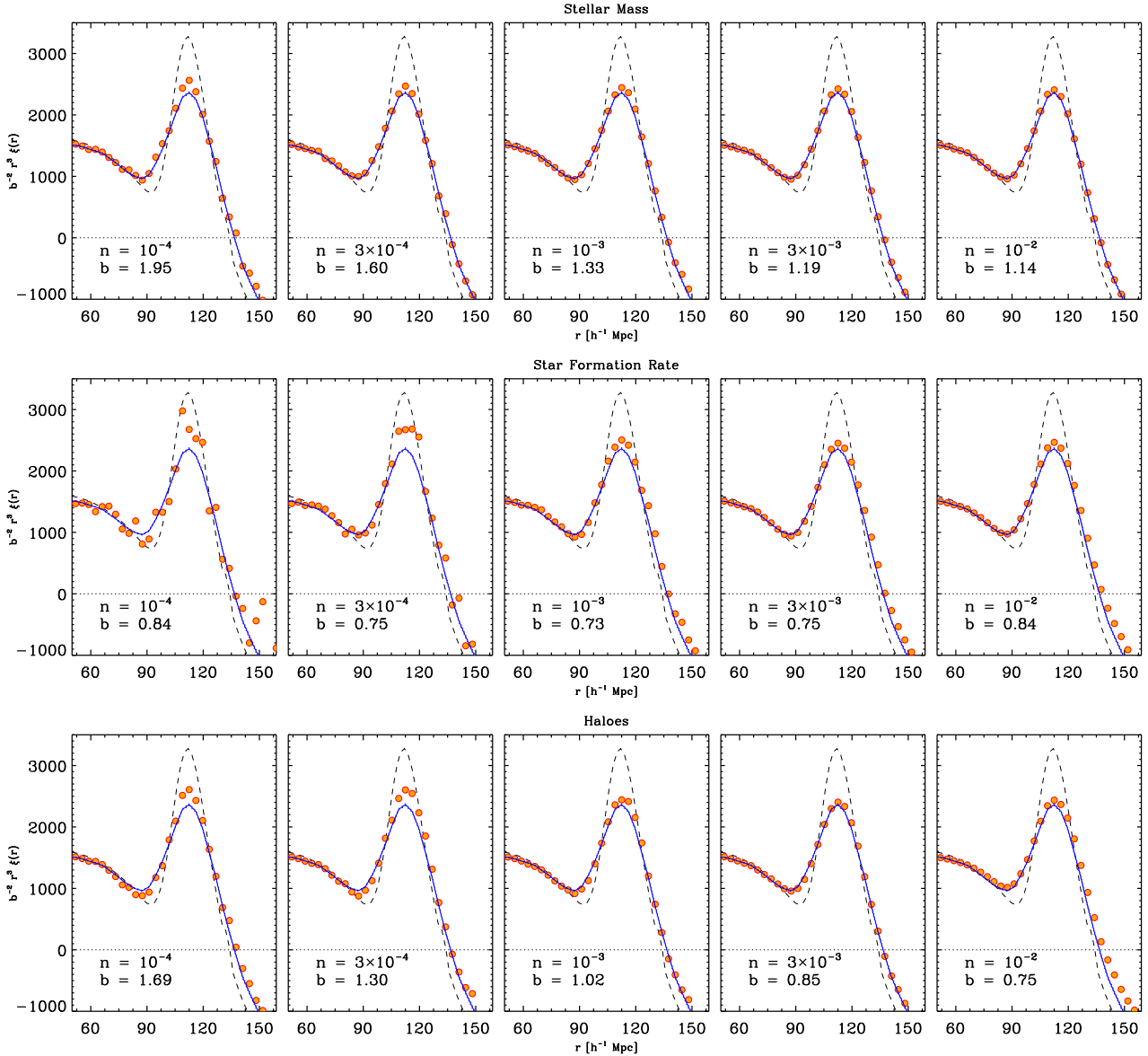
### 4.1 The BAO peak in the galaxy correlation function

Fig. 10 shows the  $z = 0$  autocorrelation functions (2pCF) predicted by our galaxy formation model for the different samples described in Section 3.2. Filled circles show results for galaxy samples selected according to stellar mass (top panel) and according to instantaneous star formation rate (middle panel). For comparison, we also show results for mass-selected halo samples (bottom panel). Each column corresponds a different number density, as indicated by the legend.

Note that we display  $r^3 \times \xi(r)$  in order to focus on the BAO signal, which appears at  $r \sim 110h^{-1}\text{Mpc}$  for our choice of cosmological parameters. In addition, in this plot we have taken out the effects of a scale-independent bias by dividing the  $y$ -axis by the ratio between the galaxy and DM 2pCF's, averaged over the range  $60 < r/h^{-1}\text{Mpc} < 70$ . Finally, for comparison we show the  $z = 0$  linear theory prediction for the 2pCF (dashed line) as well as the actual  $z = 0$  2pCF for the DM in the full MXXL (blue line).

In all galaxy samples we can identify the acoustic peak at high signal-to-noise. The large volume sampled by the MXXL,  $V = 27(h^{-1}\text{Gpc})^3$ , results in very small cosmic variance errors, and the remaining statistical fluctuations arise primarily from shot noise (i.e. Poisson noise reflecting the finite number of objects in our samples). For this reason, the scatter in our measurements decreases from left to right, and it is larger in the top panels than in the middle ones. At a fixed number density, SFR-selected galaxies cluster considerably more weakly than stellar-mass-selected galaxies (c.f. Fig. 9), so that the signal-to-noise is lower and the data points display larger random fluctuations.

All measured 2pCFs differ substantially from linear theory expectations (the dashed lines), even on these large scales. This effect has been discussed by many authors for the DM and halo distributions. It reflects nonlinear coupling of (initially independent) Fourier modes, which smears out the BAO peak (e.g. Seo & Eisenstein 2003; Angulo et al. 2005, 2008a; Crocce & Scoccimarro 2008). Here, we show



**Figure 10.** The correlation function of galaxies in the MXXL at  $z = 0$  in real space. In the top row, galaxies have been selected according to their stellar mass, in the middle row according to their instantaneous star formation rate. The bottom row displays a catalogue of DM haloes selected according to virial mass  $M_{200}$ . The bias,  $b$ , and number density of each sample (in units of  $h \text{ Mpc}^{-3}$ ) is given in the legend. Note that we display  $\xi(r) \times r^3 \times b^{-2}$  on the  $y$ -axis to enhance the acoustic peak and to take out the impact of a linear bias. For comparison, in each panel we display the 2pCF of the DM (blue solid lines) and the linear theory prediction (dashed lines).

that this effect is also visible in the galaxy distribution and that, to lowest order, it has the same magnitude in all samples, independent of their bias or number density. However, upon closer inspection, we see that significant differences are present in the amplitude of the BAO peak. We investigate this further in the next figure.

Fig. 11 displays the difference between the 2pCF of each galaxy sample and that of a linearly biased version of the DM 2pCF:  $\Delta\xi = \xi_{g,g} - b_0\xi_{m,m} = [b(r)^2 - 1]\xi_{m,m}$ , with  $b(r) = \xi_{g,m}/\xi_{m,m}$ , where  $\xi_{m,m}(r)$  is the DM autocorrelation and  $\xi_{g,m}(r)$  is the cross-correlation between DM and galax-

ies.<sup>2</sup>  $b_0$  is set to the average value of  $b(r)$  in the range  $r = [60 - 70]h^{-1}\text{Mpc}$ . We display  $10^4 b_0^{-2} D(z)^{-2} \Delta\xi$  in order to facilitate the comparison across different redshifts and bias values. Each panel focuses on a different combination of redshift and selection criterion. Within each panel, lines with different colours show results for samples of different density, as indicated by the legend. We highlight the position of the BAO peak using a vertical dashed line. Error bars are set by the diagonal elements of the cross-correlation

<sup>2</sup> We have explicitly checked that on large scales, the shape and amplitude of the scale dependent bias derived from cross- and auto-correlation functions agree extremely well.

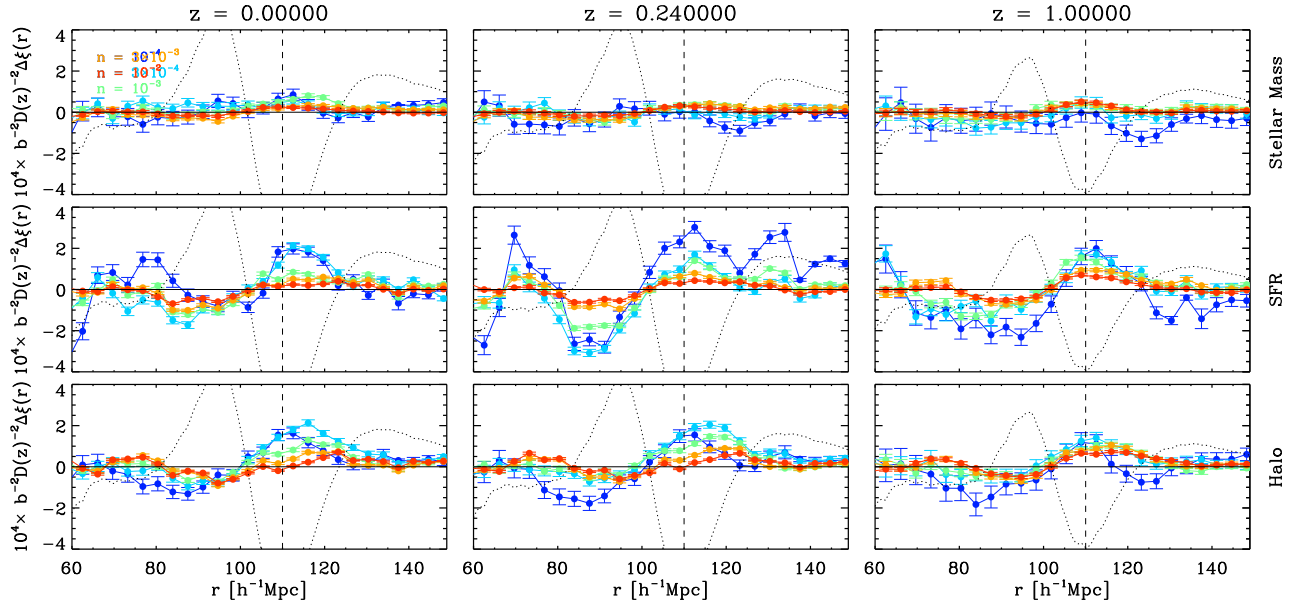


**Figure 11.** Scale dependence of the bias for galaxy samples selected according to stellar mass (top row) and to star formation rate (middle row), as well as for a mass-selected halo sample (bottom row). Coloured lines show results for samples at five different number densities, as indicated by the legend, matching the samples shown Fig.10. Vertical dashed lines denote the position of the BAO peak in the correlation function of dark matter. Deviations from zero imply deviations from linear biasing of the nonlinear dark matter distribution. The error bars are given by the square root of the diagonal elements of the covariance matrix for each measurement.

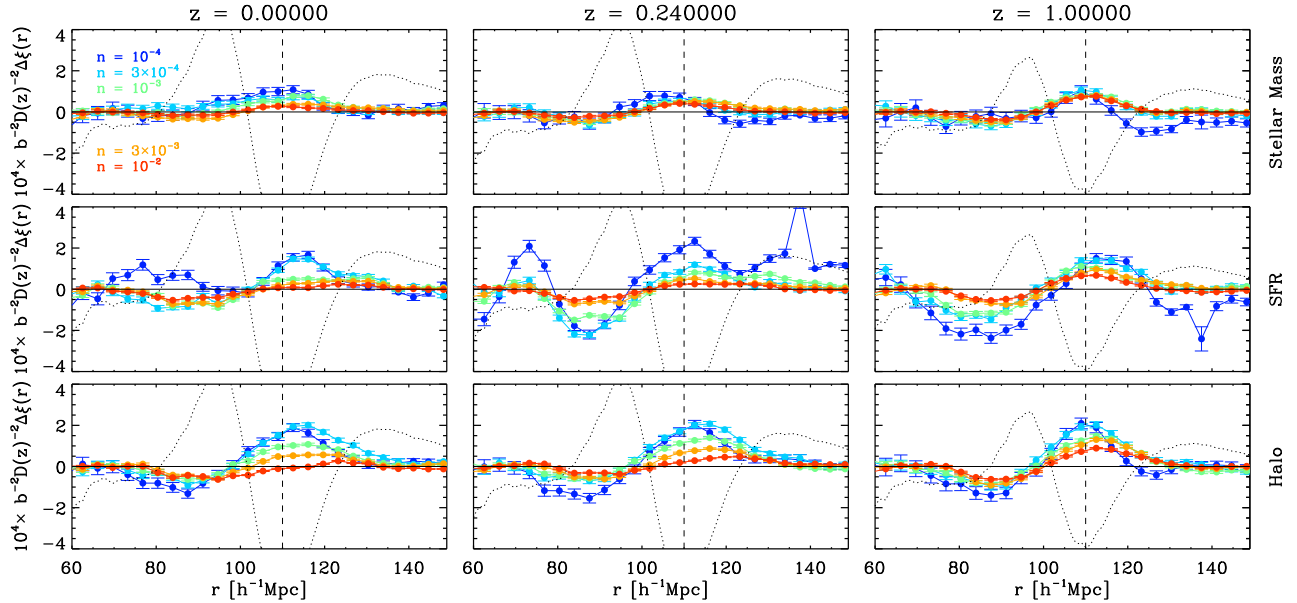


**Figure 12.** Same as Fig. 11 but for the monopole of the redshift-space correlation function.

covariance matrix, which we compute analytically following Smith (2009), including the effects of finite volume and finite tracer number. For comparison, we also overplot the difference between the linear and nonlinear DM 2pCF.

We highlight two facts that allow us to explore our results with high precision. By defining  $b(r)$  using the measured DM 2pCF at the relevant redshift, our results are essentially cosmic-variance-free. Further, the use of cross-

correlations (instead of autocorrelations) greatly suppresses the impact of shot-noise in our results (Gao & White 2007; Angulo et al. 2008b; Smith 2009). This is thanks to the large number of simulation particles in the MXXL. We note that some residual noise is still present even in the Gaussian case (Smith 2009).

We recall that if our samples were simply linearly biased versions of the underlying DM field, then all curves would

lie on top of the horizontal line, i.e. they would be equal to zero on all scales. It is clear, however, that this is not true, and systematic deviations from zero appear at many scales, most prominently at the location of the BAO peak. Quantitatively, our measurements are inconsistent with the linear bias hypothesis at the  $5 - 20\sigma$  level, as computed using the full covariance matrices. The deviations show a similar structure in most samples: by construction, they are consistent with zero at  $r \sim 60 - 70 h^{-1} \text{Mpc}$ . They show a suppression at  $r \sim 90 h^{-1} \text{Mpc}$  followed by an excess at  $r \sim 110 h^{-1} \text{Mpc}$  (the BAO peak) of slightly higher amplitude. On larger scales, they seem to approach zero again. The deviations appear to show systematic differences in shape and amplitude between the three different kinds of sample. In particular, the deviations appear to have lower amplitude for the mass-selected galaxies than for the SFR-selected galaxies or the mass-selected haloes. Also, at  $z = 0$  and  $z = 0.24$ , there is a trend with halo mass, where a lower mass threshold (i.e. a higher number density) results in a smaller deviation from zero, compared to more massive and less abundant haloes.

In Fig. 12 we show an analogous plot but this time focusing on the monopole of the redshift-space 2pCF. For this, we have employed a plane-parallel approximation, and the position along the  $z$ -direction includes the contribution of peculiar velocities. Thus, this is closer to the observed galaxy correlation function. As in the previous plot, we display results using the cross-correlation of the galaxy and dark matter field, both measured in redshift space. Here, there are also deviations from the linear bias model, indicating scale-dependent bias at the BAO position. These deviations show a structure and amplitude consistent with those in real space. In both cases, the net effect of galaxy formation appears to be an enhancement of the BAO peak. We note that the deviations are opposite to those caused by nonlinear evolution or RSD, which decrease the contrast of the BAO peak.

#### 4.2 Scale-dependent bias of galaxies and haloes

As we have discussed before, the galaxies in our model relate in a nontrivial way to the DM field. In particular, galaxy properties depend not only on halo mass but also on the details of halo accretion and merger histories, which in turn are related to halo environment. There are many effects that could produce the BAO distortions seen previously. As a test, we have "shuffled" the galaxy catalogues as in Croton et al. (2007): we randomly reassign the galaxy populations among haloes of a given mass by taking all the galaxies from halo A (including the central one) and putting them in halo B using the original halo B central galaxy position and velocity, but the properties and position/velocity offsets from halo A. This procedure guarantees that the HOD of the shuffled catalogue is identical to that of the original simulation (including all count moments, statistical fluctuations, internal spatial and velocity distributions and deviations from sphericity/isotropy) but it eliminates any spatial correlation between the populations of disjoint haloes.

We have created 100 of these shuffled catalogues to assess the associated noise. For each of them we measured the 2pCFs and computed the deviations from a linear bias model in the same way as in our original catalogues (shown

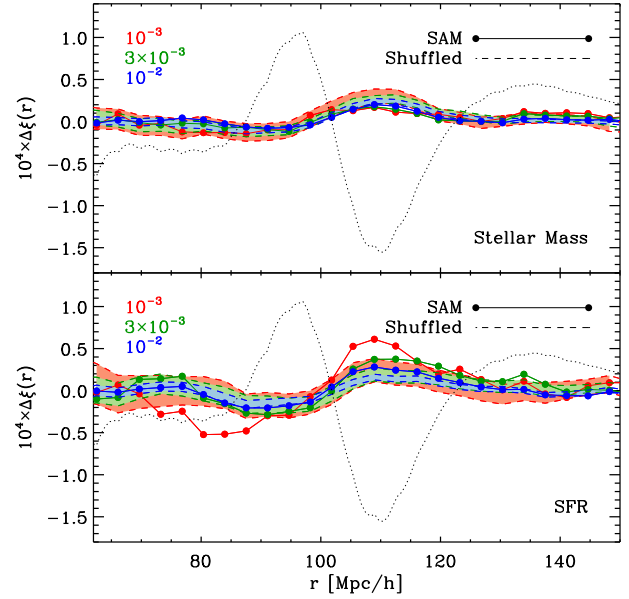


**Figure 13.** The scale-dependent distortions in the large-scale clustering of galaxies at  $z = 1$ , for two models of galaxy formation and for three samples of different number density. Solid lines show results from our original semi-analytic galaxy formation model (SAM), whereas dashed lines show results for a Halo Occupation Distribution (HOD) model built by shuffling the SAM galaxies among haloes at fixed halo mass. Filled regions show the  $rms$  scatter among 100 realisations of the shuffled catalogue.

in Figs. 11 and 12). If the clustering of galaxies is adequately described by an HOD model based on halo mass alone, then the scale-dependent bias found for the original simulation should be statistically consistent with that found for the ensemble of shuffled catalogues. A systematic difference would imply that additional variables than halo mass are important.

Fig. 13 shows our results in real space. For clarity, we display only the three highest number densities and restrict ourselves to  $z = 1$ . At other redshifts and at lower number density, the noise in the measurements is too large for robust conclusions. The upper and lower panels show results for galaxy samples selected by stellar mass and by SFR respectively. Filled circles show the measurements for the original catalogues, whereas shaded regions show the  $rms$  scatter among the results for the 100 shuffled catalogues. Although not shown here, we have checked that very similar results are found in redshift space.

In all samples, the deviations from zero have similar shape in the original and in the shuffled catalogues. The disagreements are nowhere statistically significant when galaxies are selected by stellar mass. Interestingly, however, a significant effect does appear to be present when galaxies are selected by star formation rate, although it is quite weak at high sample densities. To the accuracy of our present results, the distortion of the BAO peak appears to be adequately accounted for by an appropriate HOD model, with the possible exception of SFR-selected samples of relatively low density. We note that Eisenstein et al. (2007), Mehta et al. (2011), Wang & Zhan (2013) and Angulo et al. (2013a) have all re-



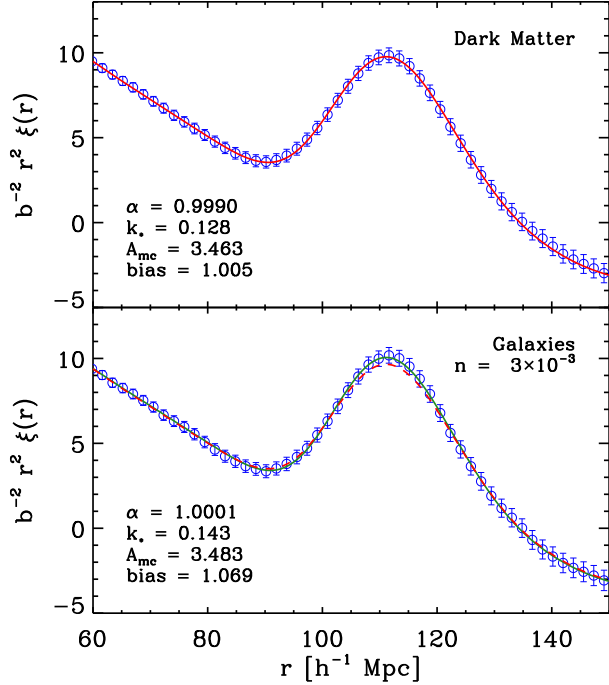


**Figure 14.** Correlation functions for DM (top panel) and for a SFR-selected galaxy sample (bottom panel), together with the best fit model (solid lines) provided by Eq. (2). Error bars are given by the square root of the diagonal elements of the respective covariance matrices. The DM correlation is repeated in the lower panel as a dashed line.

ported detections of scale-dependent bias at the BAO location for halo catalogues analogous to the one analysed here, and indeed such distortions are expected from theoretical arguments based on the peak-background split formalism (Desjacques 2008; Desjacques et al. 2010).

Although galaxy formation physics appears not to introduce further distortions in the BAO peak beyond those already present in the halo distribution, astrophysical processes do affect the peak by setting the HOD. Incorporating these effects directly in modelling of the BAO peak would require *a priori* knowledge of the HOD of the target galaxy sample, and of its evolution with redshift. This is because, as we have shown above, the deviations from a linear bias are different for halos of different mass. In principle, this information can be extracted from the observational data, but this will result in weakening, and possibly in biasing, of the constraints on cosmological parameters. We will explore this in the next subsection.

### 4.3 Biases in cosmological parameter constraints

We now quantify the impact of scale-dependent galaxy bias on future cosmological constraints. For this, we have fitted a four parameter model (similar to those applied in the analysis of real data) to our correlation function measurements. We follow Sánchez et al. (2008), who proposed a model for the shape of the galaxy correlation based on renormalised perturbation theory (Croce & Scoccimarro 2008).

This model has been applied to real data several times (e.g. Sánchez et al. 2009, 2012), and it reads as following:

$$\hat{\xi}_g(r) = b^2 [\xi_L(\alpha r) \otimes e^{-(k_* r)^2} + A_{MC} \xi'_L(\alpha r) \xi_L^{(1)}(\alpha r)] \quad (2)$$

where  $\otimes$  denotes a convolution,  $\xi'_L$  is the derivative of the linear theory correlation function, and  $\xi_L^{(1)}$  is defined as:

$$\xi_L^{(1)} = 4\pi \int P_L(k) j_1(kr) k dk, \quad (3)$$

where  $j_1(kr)$  is the spherical Bessel function of the first kind. The free parameters of the model are  $(b, k_*, A_{MC}, \alpha)$  where  $b$  is the sample bias,  $k_*$  and  $A_{MC}$  control the amount of nonlinear evolution, and  $\alpha$  is a “stretch” parameter that accounts for possible shifts in the BAO peak position due to effects not modelled, for example, scale-dependent bias. If  $\alpha$  is unity, the fitting provides unbiased measurements of the BAO location and thus of the associated distance scale. If  $\alpha \neq 1$ , then biased distances and cosmological constraints will result. We note that similar approaches based on a “stretch” parameter have been employed in the past to quantify the cosmological biases introduced by nonlinear evolution and redshift-space distortions (e.g. Seo & Eisenstein 2007; Angulo et al. 2008a; Sánchez et al. 2008).

We find the set of best fit parameters,  $(\alpha, k_*, A_{MC}, b)$ , using a Monte Carlo Markov Chain (MCMC) algorithm (with 20,000 steps) that minimises a  $\chi^2$  function over separations  $r = [70 - 140]h^{-1}\text{Mpc}$ :

$$\chi^2 = [\xi_g(\mathbf{r}) - \hat{\xi}_g(\mathbf{r})]^T C^{-1}(\mathbf{r}, \mathbf{r}') [\xi_g(\mathbf{r}') - \hat{\xi}_g(\mathbf{r}')], \quad (4)$$

where  $C^{-1}(\mathbf{r}, \mathbf{r}')$  is the inverse of the relevant covariance matrix. We estimate  $C$  analytically as described in Sánchez et al. (2008), including the effects of cosmic variance, shot-noise, galaxy bias, and correlation function binning. As discussed by Sánchez et al. (2008), this approach closely agrees with the covariance matrix measured from simulations. Finally, we note that for the input linear theory correlation function,  $\xi_L$ , we have used a  $z = 10$  measurement of the actual DM field in the MXXL simulation. In this way, we minimize the impact of cosmic variance on our best fit values. In addition, we note that predictions for galaxy 2pCF’s were constructed by cross-correlating simulated galaxies with DM particles in the MXXL. In this way, we minimize the impact of shot noise in our results.

In Fig. 14 we show the quality of the fit for two cases at  $z = 1$  in redshift space. The top panel shows the 2pCF for DM and the bottom the 2pCF for a SFR-selected galaxy sample with a number density  $n = 3 \times 10^{-4} h^{-3} \text{Mpc}^{-3}$ . We recall that the latter can be regarded as representing the expected results from the EUCLID satellite. Error bars correspond to the diagonal elements of the relevant covariance matrix. The best fit model is shown by solid lines, and the best fit parameters appear in the legend. For comparison, in the bottom panel we show the best fit for the DM as a dashed line.

In both cases, the model provides an excellent description of the data, resulting in very low values for the reduced  $\chi^2$ . However, the best fit itself is different in the two cases, as can be seen by comparing the solid and dashed lines in the bottom panel. This disagreement could lead to bias in

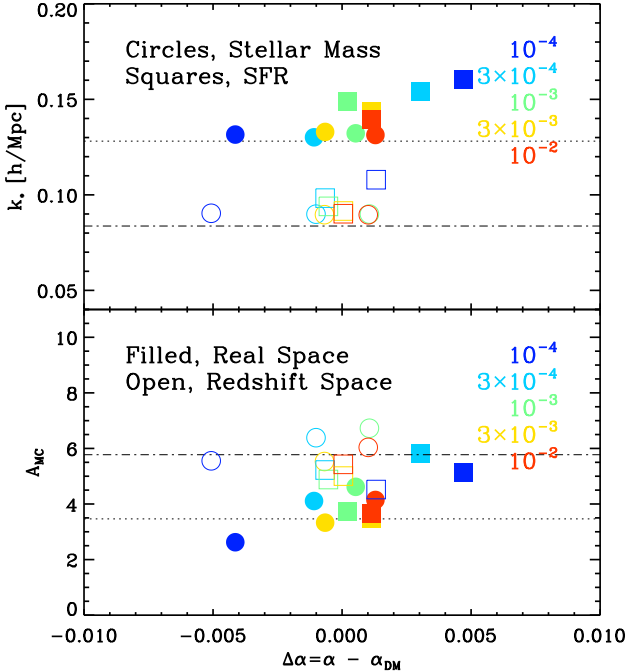


**Figure 15.** The best fit values for  $\Delta\alpha$  and  $k_*$ , and for  $\Delta\alpha$  and  $A_{\text{MC}}$  for various simulated galaxy samples. Colours indicate samples of different number density. Open and filled symbols indicate results in real and redshift space, respectively. Squares and circles indicate selection by SFR and by stellar mass, respectively. Note the  $x$ -axis displays the difference with respect to the DM best fit value. Horizontal dotted (dot dashed) lines indicate the best fit  $k_*$  and  $A_{\text{MC}}$  values for the DM correlation functions in real (redshift) space.

cosmological constraints, or it could be absorbed by another parameter of the model. The latter is indeed a reasonable expectation. Since galaxy formation effects appear with similar strength (but opposite sign) to nonlinear evolution and RSD effects, the model may absorb them by assigning slightly larger values to the  $k_*$  parameter. We explore this next.

In Fig. 15 we compile the best fit parameters  $\alpha$  and  $k_*$  (top panel); and  $\alpha$  and  $A_{\text{MC}}$  (bottom panel), for all the galaxy samples we have considered so far: selected according to SFR (circles) or stellar mass (squares), and in real (open symbols) or redshift space (filled symbols). We focus on  $z = 1$  since it is the target redshift of future large-scale surveys. The  $x$ -axis shows the differences with respect to the best fit  $\alpha$  parameter for the DM autocorrelations ( $0.99903 \pm 0.0028$  and  $1.0004 \pm 0.0035$  for the real and redshift space cases, respectively). By displaying  $\Delta\alpha$ , we take out deviations from unity resulting from residual cosmic variance and from shortcomings of the model when describing the nonlinear DM correlation function. The best fit DM  $k_*$  and  $A_{\text{MC}}$  values are indicated by the horizontal dotted lines.

As expected, values of  $k_*$  for redshift space are smaller than those for real space. Nonlinear RSD further weaken correlations, washing out the BAO peak and inducing a damping term which affects larger scales. This is seen both for DM and for our galaxy samples, independent of their number density. Values for  $A_{\text{MC}}$ , which are mostly constrained

by small separations, range from 3 to 7 and do not differ significantly between real and redshift space. These best fit values are consistent with previous studies (Sánchez et al. 2008).

The deviations of best fit values for  $\alpha$  with respect to the DM case is for the three densest galaxy samples smaller than  $\pm 0.2\%$ , and smaller than 0.5% for the two lowest density samples. This is below the target accuracy of most future surveys. The deviations from the unbiased case,  $\Delta\alpha = 0$ , show almost no correlation with  $A_{\text{MC}}$ , or  $k_*$ , and they also seem to be independent of the galaxy sample considered. For the lowest density sample, the deviations are negative when the stellar mass is used to select galaxies, and positive when the SFR is used, which suggest that it has a statistical origin. Note that the deviations from a linear bias we observe at  $z = 1$  are typically larger than those observed at lower redshifts.

As speculated above, scale-dependent biases can indeed be absorbed by the free parameters of the fitting model. In particular, in all cases, and in both real and redshift space, the best fit value for  $k_*$  is slightly larger than that measured for the DM field. This is consistent with the nature of the scale-dependent bias we measured in the previous section: the net effect is to enhance the contrast of the BAO peak, which is the opposite of nonlinear broadening of the peak, and thus a larger value for  $k_*$  is needed. These are encouraging results for future missions, in particular, for the galaxy sample matching that planned for EUCLID, we detect deviations of 0.1%, confirming that current modelling techniques are sufficiently accurate and flexible to properly exploit future BAO measurements. Nevertheless, propositions to employ the BAO damping scale to constrain cosmological parameters or modified gravity theories (e.g. Cervantes et al. 2012) could be seriously limited by the galaxy formation effects discussed here.

## 5 CONCLUSIONS

The measurement of distances in the Universe via the BAO peak is currently one of the most promising ways of constraining the cosmic expansion history. This is, in part, thanks to the theoretical understanding, quantification and correct modelling of nonlinear evolution and redshift-space distortions, effects that modify the appearance of the BAO peak in the galaxy distribution.

In this paper we have explored the impact of galaxy formation physics on the detectability and modelling of the BAO peak. Our approach followed self-consistently the evolution of over a billion galaxies in a  $70 \text{ Gpc}^3$  volume. We detect at high significance a scale-dependent bias at the BAO location, which has the net effect of enhancing the BAO contrast. We showed that the main agent causing this was already present in the halo distribution, with galaxy formation adding negligible effects for stellar mass selected samples and small effects for SFR-selected samples. Although galaxy formation physics does not add a significant extra effect, it does enter the problem indirectly by setting the halo occupation distribution, and thus the effective magnitude for the scale-dependent bias.

Although current models to extract cosmological constraints from the BAO were not designed to account explic-

itly for such scale-dependent biases, we show that they do indeed have enough flexibility to absorb these distortions in other nuisance parameters and to return measurements for the BAO location which are unbiased at the 0.2% level for most galaxy samples at  $z = 0$ . This is fortunate news for future galaxy surveys and confirms the robustness of the BAO peak and its potential as a standard ruler.

We note that our galaxy formation modelling is still simplified in many respects, and our conclusions are valid only within our specific model of galaxy formation. Although this is one of the most sophisticated and realistic prescriptions that can currently be applied to DM-only simulations, there are a number of assumptions and simplifications that may not hold in reality. In particular, the modifications to the semi-analytic model described in Section 2.2 will reduce correlations between galaxy properties and environment. Another limitation is that our modelling technique forces us to neglect the back-reaction that baryons exert on the DM distribution. Similarly, we have assumed that the density evolution of baryons and DM is identical, which is certainly not true in detail (Angulo et al. 2013b; van Daalen et al. 2013). All these effects are expected to be smaller than the ones discussed in this paper, but as the precision of measurements and our physical understanding of galaxy formation continue to improve, we may expect that yet larger and more sophisticated simulations will be needed to support robust and precise estimation of cosmological parameters from galaxy surveys.

## ACKNOWLEDGEMENTS

We would like to thank Ariel Sanchez for several useful suggestions and comments on the manuscript. Financial support from the Deutsche Forschungsgemeinschaft through Transregio 33, “The Dark Universe”, is acknowledged. RA, BH and SW acknowledge support from ERC Advanced Grant 246797 “GALFORMOD”.

## REFERENCES

- Anderson L. et al., 2012, *MNRAS*, 427, 3435  
 Angulo R., Baugh C. M., Frenk C. S., Bower R. G., Jenkins A., Morris S. L., 2005, *MNRAS*, 362, L25  
 Angulo R. E., Baugh C. M., Frenk C. S., Lacey C. G., 2008a, *MNRAS*, 383, 755  
 Angulo R. E., Baugh C. M., Frenk C. S., Lacey C. G., 2013a, *ArXiv e-prints*  
 Angulo R. E., Baugh C. M., Lacey C. G., 2008b, *MNRAS*, 387, 921  
 Angulo R. E., Hahn O., Abel T., 2013b, *MNRAS*, 434, 1756  
 Angulo R. E., Springel V., White S. D. M., Cole S., Jenkins A., Baugh C. M., Frenk C. S., 2012a, *MNRAS*, 425, 2722  
 Angulo R. E., Springel V., White S. D. M., Jenkins A., Baugh C. M., Frenk C. S., 2012b, *MNRAS*, 426, 2046  
 Angulo R. E., White S. D. M., 2010, *MNRAS*, 401, 1796  
 Baugh C. M., 2006, *Reports of Progress in Physics*, 69, 3101  
 Beutler F. et al., 2011, *Monthly Notices of the Royal Astronomical Society*, 416, 3017  
 Beutler F. et al., 2012, *MNRAS*, 423, 3430  
 Blake C. et al., 2011, *Monthly Notices of the Royal Astronomical Society*, 415, 2892  
 Bower R. G., Coles P., Frenk C. S., White S. D. M., 1993, *ApJ*, 405, 403  
 Boylan-Kolchin M., Springel V., White S. D. M., Jenkins A., Lemson G., 2009, *MNRAS*, 398, 1150  
 Cacciato M., van den Bosch F. C., More S., Mo H., Yang X., 2013, *MNRAS*, 430, 767  
 Cervantes V. D. V., Marulli F., Moscardini L., Baldi M., Cimatti A., 2012, *ArXiv e-prints*  
 Cole S. et al., 2005, *MNRAS*, 362, 505  
 Crocce M., Scoccimarro R., 2008, *Phys. Rev. D*, 77, 023533  
 Croton D. J., Gao L., White S. D. M., 2007, *MNRAS*, 374, 1303  
 Davis M., Efstathiou G., Frenk C. S., White S. D. M., 1985, *ApJ*, 292, 371  
 Desjacques V., 2008, *Phys. Rev. D*, 78, 103503  
 Desjacques V., Crocce M., Scoccimarro R., Sheth R. K., 2010, *Phys. Rev. D*, 82, 103529  
 di Porto C., Amendola L., Branchini E., 2012, *MNRAS*, 419, 985  
 Drinkwater M. J. et al., 2010, *MNRAS*, 401, 1429  
 Eisenstein D. J., Seo H., Sirko E., Spergel D. N., 2007, *The Astrophysical Journal*, 664, 675  
 Eisenstein D. J. et al., 2011, *AJ*, 142, 72  
 Eisenstein D. J. et al., 2005, *ApJ*, 633, 560  
 Fu L. et al., 2008, *A&A*, 479, 9  
 Gao L., Springel V., White S. D. M., 2005, *MNRAS*, 363, L66  
 Gao L., White S. D. M., 2007, *MNRAS*, 377, L5  
 Guo Q., White S., Angulo R. E., Henriques B., Lemson G., Boylan-Kolchin M., Thomas P., Short C., 2013a, *MNRAS*, 428, 1351  
 Guo Q. et al., 2011, *MNRAS*, 413, 101  
 Guo Q. et al., 2013b, *MNRAS*, 435, 897  
 Guo Q., White S. D. M., 2008, *MNRAS*, 384, 2  
 Henriques B. M. B., White S. D. M., Lemson G., Thomas P. A., Guo Q., Marleau G.-D., Overzier R. A., 2012, *MNRAS*, 421, 2904  
 Hill G. J. et al., 2008, in *Astronomical Society of the Pacific Conference Series*, Vol. 399, *Panoramic Views of Galaxy Formation and Evolution*, Kodama T., Yamada T., Aoki K., eds., p. 115  
 Kim J., Park C., Rossi G., Lee S. M., Gott, III J. R., 2011, *Journal of Korean Astronomical Society*, 44, 217  
 Komatsu E. et al., 2011, *ApJS*, 192, 18  
 Laureijs R., 2009, *ArXiv e-prints*, astro-ph/0912.0914  
 Mehta K. T., Seo H.-J., Eckel J., Eisenstein D. J., Metchnik M., Pinto P., Xu X., 2011, *ApJ*, 734, 94  
 Planck Collaboration et al., 2013, *ArXiv:1303.5076*  
 Rozo E. et al., 2010, *ApJ*, 708, 645  
 Sánchez A. G., Baugh C. M., Angulo R. E., 2008, *MNRAS*, 390, 1470  
 Sánchez A. G., Crocce M., Cabré A., Baugh C. M., Gaztañaga E., 2009, *MNRAS*, 400, 1643  
 Sánchez A. G. et al., 2012, *MNRAS*, 425, 415  
 Seo H.-J. et al., 2010, *ApJ*, 720, 1650  
 Seo H.-J., Eisenstein D. J., 2003, *ApJ*, 598, 720  
 Seo H.-J., Eisenstein D. J., 2005, *ApJ*, 633, 575  
 Seo H.-J., Eisenstein D. J., 2007, *ApJ*, 665, 14  
 Simha V., Cole S., 2013, *MNRAS*  
 Smith R. E., 2009, *MNRAS*, 400, 851

- Smith R. E., Scoccimarro R., Sheth R. K., 2008, Phys. Rev. D, 77, 043525
- Springel V. et al., 2005, Nature, 435, 629
- Suzuki N. et al., 2012, ApJ, 746, 85
- Vale A., Ostriker J. P., 2004, MNRAS, 353, 189
- van Daalen M. P., Schaye J., McCarthy I. G., Booth C. M., Dalla Vecchia C., 2013, ArXiv e-prints
- Viel M., Becker G. D., Bolton J. S., Haehnelt M. G., 2013, Phys. Rev. D, 88, 043502
- Wang Q., Zhan H., 2013, ApJ, 768, L27
- Wang W., White S. D. M., 2012, MNRAS, 424, 2574
- Watson W. A., Iliev I. T., Diego J. M., Gottlöber S., Knebe A., Martínez-González E., Yepes G., 2013, ArXiv e-prints
- Wechsler R. H., Zentner A. R., Bullock J. S., Kravtsov A. V., Allgood B., 2006, ApJ, 652, 71